Fermi arc mediated entropy transport in topological semimetals

Timothy M. McCormick, Sarah J. Watzman, Joseph P. Heremans, and Nandini Trivedi

Phys. Rev. B **97**, 195152 — Published 29 May 2018

DOI: 10.1103/PhysRevB.97.195152

Fermi arc-mediated entropy transport in topological semimetals

Timothy M. McCormick,[1,*] Sarah J. Watzman,[2] Joseph P. Heremans,[1,2,3] and Nandini Trivedi[1,†]

[1] *Department of Physics and Center for Emergent Materials, The Ohio State University, Columbus, OH 43210, USA*
[2] *Department of Mechanical and Aerospace Engineering, The Ohio State University, Columbus, Ohio 43210, USA*
[3] *Department of Materials Science and Engineering, The Ohio State University, Columbus, Ohio 43210, USA*

(Dated: April 25, 2018)

The low energy excitations of topological Weyl semimetals are comprised of linearly dispersing Weyl fermions that act as monopoles of Berry curvature in the bulk momentum space. Furthermore, on the surface there exist topologically protected Fermi arcs at the projections of these Weyl points. We propose a novel pathway for entropy transport involving Fermi arcs on one surface connecting to Fermi arcs on the other surface via the bulk Weyl monopoles. We present results for the temperature and magnetic field dependence of the magnetothermal conductance of this conveyor belt channel. The circulating currents result in a net entropy transport without any net charge transport. We provide results for the Fermi arc-mediated magnetothermal conductivity in the low-field semiclassical limit as well as in the high-field ultra-quantum limit, where only chiral Landau levels are involved. Our work provides the first proposed signature of Fermi arc-mediated magnetothermal transport and sets the stage for utilizing and manipulating the topological Fermi arcs in thermal applications.

INTRODUCTION

It is now well understood that topological insulators are protected by a gap in the bulk and necessarily have topological surface states arising from the bulk-boundary correspondence [1, 2]. The recent theoretical prediction [3–6] and subsequent experimental discovery [7–9] of Dirac and Weyl semimetals (WSMs) have expanded this list of topological quantum materials to include semimetals with no bulk band gap. WSMs possess nodal fermions comprised of non-degenerate linear band crossings. In order to satisfy the condition of non-degeneracy, WSMs must break either inversion-symmetry or time-reversal symmetry. The Weyl nodes come in pairs of opposite chirality [10], and, unlike Dirac fermions in graphene [11], they are robust against the formation of a gap due to their three-dimensional nature.

The low energy linear dispersing modes of a WSM carry monopole charges of Berry curvature concentrated at the Weyl nodes leading to predictions of novel electronic transport [12–20]. The observation of a negative longitudinal magnetoresistance [21–23] in the presence of parallel electric and magnetic fields, has been understood to arise from the chiral anomaly due to the local non-conservation of charge in the Brillouin zone.

In addition to the plethora of novel transport phenomena exhibited by WSMs, these monopole charges of Berry curvature are responsible for topological Fermi arcs in WSMs, perhaps their most fascinating feature. Fermi arcs form open contours of surface states that terminate on the projections of Weyl nodes, or in the case of doped WSMs, terminate on the projections of Fermi pockets enclosing Weyl nodes. The dispersion around the bulk nodes is linear in three dimensions. The Fermi arc states on the surface have a linear dispersion in the two dimensional surface Brillouin zone and are chiral, so that the velocity of electrons on one of the surfaces is unidirectional and is opposite on the other surface. These gapless surface modes provide the key signature for WSMs in spectroscopy experiments [7–9].

Fermi arcs in WSMs are known to lead to exotic quantum oscillations involving mixed real and momentum space orbits [24–27] as well as resonant transparency [28]. However, the effect of Fermi arcs on thermal transport so far remains an unexplored frontier. Preliminary studies of thermal transport in WSMs have so far only considered contributions from the bulk Weyl fermions [29–33]. One of the major challenges we address in this paper is: Can we find signatures of Fermi arcs in thermal transport? How can we design an experiment that isolates the effect of the arcs from all of the other contributions, such as the bulk monopoles, ambipolar transport from electron and holes around the Weyl points, and all of the other trivial pockets?

We predict that Fermi arc-mediated entropy transport and consequently the anisotropic magnetothermal conductivity discussed in this paper provides a unique signature of the topological Fermi arcs in WSMs. Specifically we obtain the following results:
(i) Even when transport in a magnetic field is incoherent i.e. $\omega_c\tau \ll 1$ where ω_c is the cyclotron frequency and τ is the elastic intra-valley scattering time, it is possible to get coherent entropy transport in an applied thermal gradient without any charge transport. The charge circulates like a fluid in a "conveyor belt" from the Fermi arc on the top surface, into the bulk via the Weyl node, down to the arc on the other surface and back up to the top surface via the second Weyl node. We emphasize that the "conveyor belt" transport occurs as a consequence

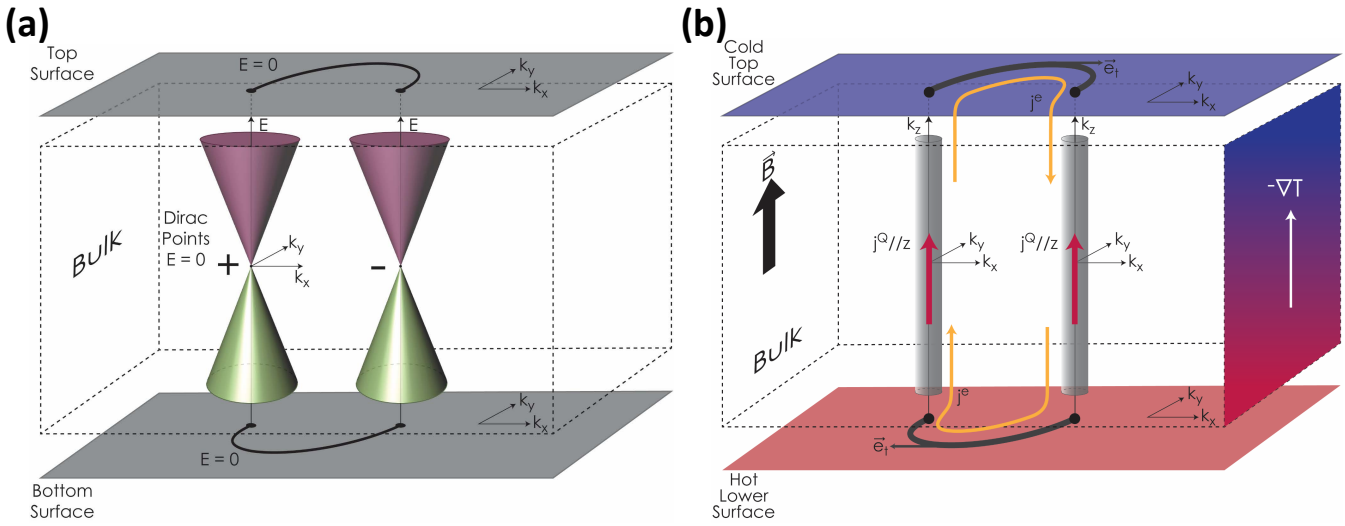

FIG. 1. (a) Mixed real-space and momentum-space depiction of a Weyl semimetal in a slab geometry with thickness L in the z-direction. Bulk Weyl nodes are labeled with their chirality $\chi = \pm$ and separated in the k_x-direction. The projections of the Weyl nodes on the surface Brillouin zone define the end points of the Fermi arcs on the top and bottom surfaces. (b) Schematic of the "conveyor belt" motion of charge leading to a net heat flux. When $\mathbf{B}$ is aligned in the z-direction in (a), charge current density circulates $\mathbf{J}^e$ in the clockwise direction shown in a mixed real and momentum space orbit. When ∇T is also aligned in the z-direction, this circulation of charge leads to a net flow of heat current density $\mathbf{J}^Q$ in the direction shown. Unit tangent vectors $\mathbf{e}_t$ are shown for the arcs.

of the continuity equation, so long as inter-nodal scattering is suppressed, and does not require quantized Landau orbits. The precise geometry is described below.

(ii) Although the "conveyor belt" allows for heat transport in the absence of charge transport, we show that Wiedemann-Franz law is obeyed in both semi-classical and ultra-quantum regimes, albeit with different Lorenz numbers, because of the different density of states.

(iii) In the low-field regime, the arc-mediated thermal conductivity $\kappa_{zzz} \propto T^3BL$ [see Eqn. (4) for the exact expression]. Note, the three directions in the tensor κ pertain to the thermal gradient, the heat current and the magnetic field, all taken to be along z and perpendicular to the separation between Weyl points along x. In the ultra-quantum limit, $\kappa_{zzz} \propto G^Q_{\rm th}B^2L$ [see Eqn. (11) for full expression], where $G^Q_{\rm th}$ is the quantum of thermal conductance[34, 35]. The arc-mediated contribution to κ can be separated from the bulk contribution by switching the magnetic field to an orthogonal direction from the thermal gradient.

To put our results in perspective, all semimetals have ambipolar (i.e. electron and hole) contributions to thermal conductivity[36]. As an example, in bismuth ambipolar conduction contributes 40% of the total thermal conductivity at $T = 200$K[37]. The conveyor belt motion of entropy that we propose is distinct from ambipolar transport. It is a topological property of the Fermi arcs of Weyl and Dirac semimetals whose driving mechanism is a combination of the Lorentz force from the magnetic field on the Fermi arcs and the conservation of charge that necessitates motion through the bulk.

We conclude by comparing the arc-mediated contribution to the thermal conductivity with the bulk contribution and show that the former dominates. We discuss the role of intra and inter-nodal elastic scattering, inelastic scattering and phonon drag, and argue that because of the limited phase space, the "conveyor belt" mechanism for entropy transport is robust. Our results have broad experimental implications for both type I and type II WSMs as well as Dirac semimetals. Our predictions provide a quintessential signature of Fermi arcs in topological semimetals. This work also sets the stage for utilizing and manipulating topological Fermi arcs in experimental magnetothermal applications and in novel tools for thermal energy conversion technology, such as magnetically driven heat switches.

FERMI ARC-MEDIATED MAGNETOTHERMAL TRANSPORT

Model

We consider a linearized model of Weyl fermions in the continuum limit. For a given Weyl node of chirality $\chi = \pm 1$, the Hamiltonian near the node is given by:

$$\hat{H}_\chi = \chi\hbar v_F\Big(k_x\hat{\sigma}_x + k_y\hat{\sigma}_y + k_z\hat{\sigma}_z\Big), \qquad (1)$$

where v_F is the Fermi velocity of the Weyl fermions and the Pauli matrices $\hat{\sigma}_j$ span either spin or orbital degree

of freedom. These Weyl nodes come in pairs of opposite chirality; we consider N_p pairs of nodes. We assume that the chemical potential lies *at* the Weyl nodes. In a real material, this is not necessarily the case, in which case the bulk Fermi surface becomes a pocket of radius $k_F = \frac{\mu}{\hbar v_F}$. At finite temperatures, the Fermi surface broadens over the energy scale $k_B T$, creating a channel of width $\Delta k \sim \frac{k_B T}{\hbar v_F}$. For simplicity, we will take all Weyl nodes to lie at the same energy $E = 0$, but our calculations generalize to cases where sets of Weyl nodes lie at different energies.

For certain parts of the analysis discussed below, it is useful to consider the following lattice model[38, 39] for a Weyl semimetal

$$\begin{aligned}\mathcal{H}_{\text{Latt}}(\mathbf{k}) = -\big(&m(2-\cos(k_y a)-\cos(k_z a))+\\ &2t_x(\cos(k_x a)-\cos(k_0 a))\big)\hat{\sigma}_x\\ &-2t\,\sin(k_y a)\hat{\sigma}_y - 2t\,\sin(k_z a)\hat{\sigma}_z,\end{aligned} \tag{2}$$

where a is the lattice spacing, k_0 sets the separation of the Weyl nodes, and t, t_z and m are parameters that determine the dispersion. The lattice model in Eqn. (2) reduces to the linearized model in Eqn. (1) for momenta below a cutoff Λ. We consider a slab geometry by Fourier transforming Eqn. (2) in the z-direction. This lattice model proves to be useful in understanding heat flow in the mixed real- and momentum-space description of the WSM.

Semiclassical Regime

We are motivated by previous studies of quantum oscillations involving mixed real and momentum space orbits[24–27] in topological semimetals. These oscillations arise due to Onsager quantization from quantum coherence of the electrons across the entire bulk-arc orbits [24]. Rather than oscillations of the density of states from the Fermi arcs, we predict that the presence of Fermi arcs will result in distinct channels of entropy transport, even in the semiclassical regime.The driving principle is the continuity equation.

In this section, we calculate the heat current flow in response to a thermal gradient and an externally applied magnetic field whose coefficient gives the magnetothermal conductivity $J^Q_\mu = \kappa_{\mu\nu\gamma}\nabla_\nu T$ and γ defines the direction of the magnetic field. In particular, we focus on the Fermi arc mediated entropy transport. We show that this heat current depends on the particle flux from the arcs through the bulk driven by a magnetic field and on the heat capacity of the bulk states. The particle current through the bulk is calculated from the continuity of charge and the Lorentz force of an external magnetic field on the arcs. We show that the particle flux results in no net charge transport, but produces a heat current in the presence of a thermal gradient. Our results for the thermal and electronic conductances can be cast transparently in the Landauer framework and show that the Wiedemann-Franz law is obeyed.

Particle flow: In an external magnetic field, charge flow is essentially governed by the Lorentz force and the continuity equation. The conservation of charge dictates that through each bulk pocket surrounding a node with chirality χ, we must have a real-space current density given by $J^e_{z;\chi} = \chi\frac{e}{A}\frac{dN}{dt}$ where $\frac{dN}{dt}$ is the flow rate to be discussed below. Fig. 1a shows a mixed real-space and momentum-space diagram of a Weyl semimetal in a slab geometry. The magnetic field induces a flow of electrons along the arcs from left to right along the Fermi arc on the top surface in Fig. 1b and similarly from right to left along the Fermi arc on the bottom surface. The only way the system can maintain a steady-state circulation of electrons and obey the continuity equation is by transporting electrons via the bulk Weyl nodes. These circulating currents are the low-field analog of magneto-oscillations explored by the authors of Ref.[24]. We predict magneto-resistance oscillations around the conveyor belt in the low-field limit as well so long as inter-nodal scattering is suppressed. Note, our argument does not require quantum coherence across the loop as the current in the semiclassical regime is directed by the continuity of charge. The total current is given by summing over all pairs of nodes and chiralities and equals zero. Thus, since Weyl nodes come in pairs of opposite chirality, the circulating currents in the steady state do not cause any net current flow along the z-direction in the absence of external potentials.

Entropy Flow: The heat current density along z for N_p pairs of Weyl nodes is given by,

$$J^Q_z = N_p\frac{1}{A}\frac{dN}{dt}\left[E\left(T(z+\frac{L}{2})\right) - E\left(T(z-\frac{L}{2})\right)\right]. \tag{3}$$

where $E(T(z))$ is the thermal energy per particle at layer z of a slab of thickness L. In the presence of only a thermal gradient, the electrons will move from the hot surface through the bulk around one node to the cold surface as described by the first term within the brackets in Eqn. (3). An additional perpendicular magnetic field $\mathbf{B} = B\mathbf{e}_z$ exerts a Lorentz force on electrons. As a result, electrons that have reached the cold surface through one of the nodes are driven along the arc to the other node and back to the top surface, described by the second term in Eqn. (3). This circulation of current occurs for arbitrarily small magnetic fields. The total heat current is then the sum of these two contributions. Note, in the absence of a magnetic field, the arcs do not contribute to the heat current in the z-direction since the Fermi velocity of electrons residing in the arcs is normal to the direction of the applied thermal gradient.

By expanding the thermal energies per particle $E(T(z \pm \frac{L}{2}))$ we obtain $J^Q_z = \frac{N_p L}{2A}\frac{dN}{dt}\frac{dE}{dT}\frac{dT}{dz}$. Each

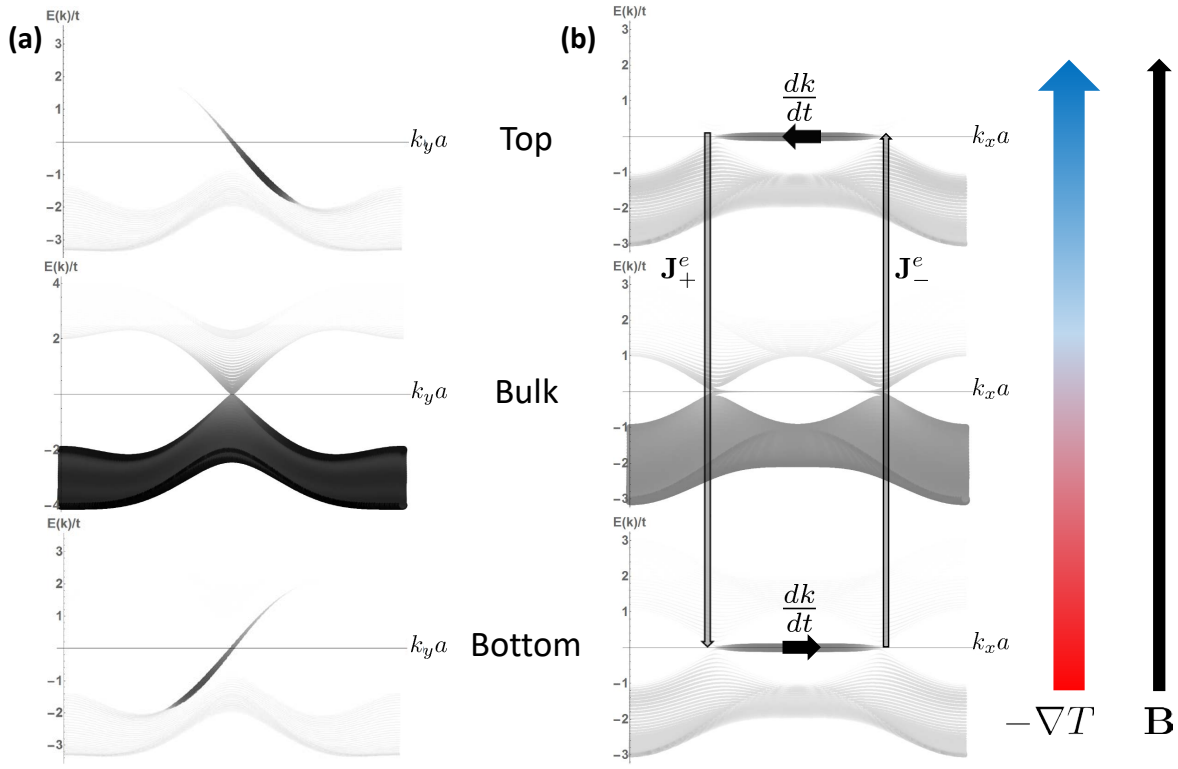

FIG. 2. (a) Thermal occupations for the minimal model in Eqn. (2) with $m = 2t$, $t_z = t$, and $k_W a = \pi/2$ for cuts along k_y at fixed $k_x a = 0.75\pi$ (top and bottom) and $k_x a = 0.5\pi$ (bulk). We show the occupations of the top two layers (top), the bottom two layers (bottom) and the other layers (bulk), weighting each point's color and thickness in the figure with the Fermi function f_0 at that layer for a temperature gradient of $\frac{dT}{dz} = \frac{0.8t}{k_B a}$ at an average temperature of $k_B T = 0.6t$. (b) Orbits for the minimal model in Eqn. (2) with the same parameters as in (a) for cuts along k_x at $k_y = 0$. We again show the occupations of the top two layers (top), the bottom two layers (bottom) and the other layers (bulk), weighting each point as in (a) with the same temperature and temperature gradient. We show the mixed real- and momentum-space orbits and see that the the states most occupied on the top and bottom are the arcs, while the bulk states merge into the arc and carry heat through the bulk.

of the variations can be estimated as follows: (a) The change in the number N of electrons on a given surface of area A with one Fermi arc $\frac{dN}{dt} = A\frac{dn}{d\mathcal{E}}\frac{d\mathcal{E}}{dk}\frac{dk}{dt}$ where the density of states of the Fermi arcs $g_A(\mathcal{E}) \equiv \frac{dn}{d\mathcal{E}} = \frac{k_0}{\hbar v_F}$ and $\frac{d\mathcal{E}}{dk} = \hbar v_F$, determined by the magnitude of the Fermi velocity v_F and the length of the Fermi arc k_0. The Lorentz force on an electron wavepacket on a Fermi arc is $\frac{d\mathbf{k}}{dt} = \frac{e}{\hbar c}(\mathbf{v_k} \times \mathbf{B}) = \frac{e}{\hbar c} v_F B \mathbf{e}_t$, where $\mathbf{e}_t$ is the unit tangent vector to the Fermi arc, and we have assumed for simplicity that the magnitude of the velocity v_F of the linearly dispersing Fermi arc states at different points along the arc is the same. Thus the total rate of electrons moving along each arc is given by $\frac{dN}{dt} = A\frac{e}{\hbar c} k_0 v_F B$. (b) The electronic heat capacity of the bulk Weyl pockets (see appendix A) $\frac{dE}{dT} = \frac{7\pi^2}{15}\frac{k_B \Lambda^3 \Theta^3}{n_B}$ in terms of a dimensionless temperature $\Theta \equiv \frac{k_B T}{\hbar v_F \Lambda}$ and density $n_B = \frac{N}{V}$.

The contribution of the Fermi arcs to the thermal conductivity is,

$$\kappa^S_{zzz} = \frac{14 N_p}{15}(k_B v_{_F} \Lambda^2)\Theta^3 \left(\frac{k_0 L}{(l_B \Lambda)^2}\right), \qquad (4)$$

where the superscript S stands for "semiclassical" to distinguish it from "ultra-quantum" that we will consider later. Since the momentum cutoff Λ provides the only length scale in this continuum limit, the density scales as $n_B \sim \Lambda^3$ and $l_B = \sqrt{\frac{\hbar c}{eB}}$ is the magnetic length. The T^3 dependence to the specific heat from Fermi arcs is analogous to that from phonons, however, the thermal conductivity of phonons should be independent of magnetic field, providing a route for separating phonon contributions from the electronic contribution of Weyl nodes.

The scale for κ in a bulk WSM is set by $k_B v_F (2\pi/a)^2 \approx 10^2$ $\mathrm{Wm^{-1}K^{-1}}$ where we have used $v_F \sim 3 \times 10^5 \frac{\mathrm{m}}{\mathrm{s}} \sim c/10^3$ and the lattice constant $a \sim 0.3$nm. The additional arc contribution is enhanced by the factor (L/l_B) where the magnetic length $l_B \approx 25\mathrm{nm}/\sqrt{B(T)[\mathrm{Tesla}]}$. For a 1 mm sample thickness in a 1 tesla magnetic field, the enhancement factor $L/l_B \sim 4 \times 10^4$ should render this

effect experimentally measurable.

We have considered the arcs to lie in a plane perpendicular to the direction of the applied magnetic field. In an inversion-breaking Weyl semimetal with time-reversal symmetry present, there is only one such plane. However, in a time-reversal breaking Weyl semimetal, arcs may exist simultaneously perpendicular and co-planar with respect to the applied magnetic field. In this case, the arcs co-planar with the field will not experience a force in the plane of the arcs. Hence, we expect that only the arcs perpendicular to the field will result in a particle flux.

We also note that, in general, there are three contributions to the thermal conductivity in a Weyl semimetal: (a) the contribution of only the bulk, (b) the contribution solely from the arcs and (c) the thermal conductivity from the mixed bulk-arc conveyor belt discussed above. The role of the bulk states has been discussed by previous work[29, 30], and we provide a detailed comparison between the bulk and the arc-driven conveyor belt thermal conductivity in a later section of this paper. The arcs themselves are strictly two-dimensional and, hence, the arcs which contribute to the thermal conductivity of the conveyor belt states will not contribute directly themselves to the thermal conductivity, since the Fermi velocity on the arcs is perpendicular to the direction of the thermal gradient and heat current. We emphasize that the direction of the Fermi velocity on the arcs is directly responsible for the conveyor belt motion discussed above.

Heat Map: In Fig. 2, we give a "heat map" for a fixed temperature gradient applied across the top and bottom surfaces around an average temperature. Such a map highlights the states that are involved in momentum space as heat flows from bottom to top in real space. In Fig. 2a, we show three cuts along k_y for the top and bottom two layers (at fixed $k_y a = 0.75\pi$) and for the bulk (at $k_y a = 0.5\pi$). We weight each point's size and color with the expectation value $\langle z \rangle$ multipled by the thermal occupancy of that state $f^0(\mathcal{E}_k) = \left(1 + e^{\frac{\mathcal{E}_k - \mu}{k_B T}}\right)^{-1}$ (we have again taken $\mu = 0$).

We see that on the "hot" end, states at higher energies have a higher thermal occupation, while on the "cold" end, states on the Fermi arcs have a lower thermal occupation. In Fig. 2b, we show three cuts along k_x at $k_y = 0$ for the top two layers, the bottom two layers, and all other layers with each point weighted as in Fig. 2a. In Fig. 2b, we also trace out the orbits shown in Fig. 1, this time overlaying them on the slab coordinates. We see that the states most occupied on the top and bottom are the arcs, while the bulk states merge into the arc and carry heat through the bulk (see supplement).

Landauer conductances: We use the Landauer formalism[41–44] to calculate the thermal $K = \frac{A}{L}\kappa$ and electrical $G = \frac{A}{L}\sigma$ conductances[45] of the arc-mediated channel and from their ratio show that the Wiedemann-Franz law holds. The thermal conductance is

$$\frac{K}{T} = 2\frac{k_B^2}{\hbar}\int d\mathcal{E}\left(\frac{\mathcal{E}-\mu}{k_B T}\right)^2\left(-\frac{\partial f_0}{\partial \mathcal{E}}\right)\mathcal{M}(\mathcal{E})\,\mathcal{T}(\mathcal{E}), \quad (5)$$

where $\mathcal{T}(\mathcal{E})$ is the transmission coefficient and $\mathcal{M}(\mathcal{E})$ is the number of propagating modes. We expand $\mathcal{M}(\mathcal{E})\,\mathcal{T}(\mathcal{E})$ in a power series, and, by evaluating Eqn. (5) and comparing it with Eqn. (4), we find that $\mathcal{M}(\mathcal{E})\,\mathcal{T}(\mathcal{E}) = N_P g_B(\mathcal{E})\frac{\hbar}{n_B}\frac{dN}{dt}$, where N_P and n_B are the number of pairs of Weyl nodes and the bulk density respectively, the bulk density of states is given by $g_B(\mathcal{E}) = \frac{1}{\pi^2}\frac{\mathcal{E}^2}{(\hbar v_F)^3}$ and $\frac{dN}{dt}$ is obtained previously.

The electrical conductance $G = \frac{A}{L}\sigma$ of the arc-mediated channel can be similarly determined by calculating

$$G = 2\frac{e^2}{\hbar}\int d\mathcal{E}\left(-\frac{\partial f_0}{\partial \mathcal{E}}\right)\mathcal{M}(\mathcal{E})\,\mathcal{T}(\mathcal{E}). \quad (6)$$

Using $\mathcal{M}(\mathcal{E})\,\mathcal{T}(\mathcal{E})$ from the argument above,

$$G^S = \frac{N_p}{3}\frac{e^2}{\hbar}g_B(\mathcal{E})\frac{\hbar}{n_B}\frac{dN}{dt}. \quad (7)$$

From Eqns. (4) and (7), we can find the Lorenz number

$$L^S = \frac{\kappa^S_{zzz}}{T\sigma^S_{zzz}} = \frac{7\pi^2}{5}\left(\frac{k_B}{e}\right)^2 \quad (8)$$

for the arc-mediated channels. We note that the dimensionless prefactor of the Lorenz number differs from its usual value of $\pi^2/3$ due to the massless Dirac nature of the Weyl nodes. We note that although the Wiedemann-Franz law holds, heat flows in the presence of a thermal gradient without a net flow of charge due to the circulating currents.

We propose that optical injection of a heat current into the conveyor belt should generate a temperature gradient according to the thermal conductivity that we predict. This thermal conductivity will be independent of scattering between arcs and leads and therefore intrinsic to the sample. The leads themselves will add a contact resistance which will enhance thermalization on the surface states.

Ultra-quantum Regime

For large magnetic fields along the z-direction, the Weyl node energies split into discrete Landau levels

shown in Fig. 3, given by

$$\mathcal{E}_n(k_z) = \chi \frac{\hbar v_F}{l_B}\sqrt{2|n| + (k_z l_B)^2}. \tag{9}$$

Due to the linear dispersion around the Weyl nodes, the Landau levels are not evenly spaced. In the ultra quantum limit, the chiral Landau level $n = 0$ in the bulk, provides a single channel for entropy and charge transport along the "conveyor belt". The sign of the slope of the $n = 0$ Landau level depends on the chirality of the Weyl node. Here, $l_B = \sqrt{\frac{\hbar c}{eB}}$ is the magnetic length, and v_F is the magnitude of the Fermi velocity.

We next investigate the heat current flow in response to an applied temperature gradient in strong applied magnetic fields. We show that the arc-mediated magnetothermal conductivity in this regime allows for a direct probe of the quantum of thermal conductance.

As an electron moves along the arc, it terminates on the projection of a Weyl node, which, in the presence of a large magnetic field, is described by Landau levels in Eqn. (9). For $k_B T \ll \frac{\hbar v_F}{l_B}$, the only state available is the zeroth Landau level. Because of the chiral nature of these states, electrons from the arc traverse the bulk without dissipation and emerge on the other surface. After it reaches the other side, it moves along another Fermi arc until it reaches the bulk Weyl node with the opposite chirality. It then traverses the bulk in the opposite direction and completes the loop.

Once again, we consider a thermal gradient in the same direction as the magnetic field along z. The conveyor belt motion of the electrons enhances the magnetothermal conductivity. However, unlike the semiclassical regime, now the $n = 0$ Landau levels provide a single quantum channel for heat transport.

The specific heat of the zeroth Landau level (see Appendix B) in the low temperature limit $\Theta \equiv \dfrac{k_B T}{\hbar v_F \Lambda} \ll 1$, is $\dfrac{dE_0}{dT} \approx \dfrac{2\pi}{3}\dfrac{n_B k_B^2}{\hbar v_F \Phi_0} TB$, where E_0 is the energy per particle of the $n = 0$ Landau level and $\Phi_0 = \frac{hc}{e}$ is the flux quantum. The continuity of charge leads to a particle current $\dfrac{dN}{dt} = A\dfrac{e}{\hbar c}k_0 v_F B$ obtained through the bulk, and by summing over the nodes, we obtain a nonzero net heat current. The resulting thermal conductivity

$$\kappa_{zzz}^{UQ} = \frac{\pi^2}{3} N_p \frac{k_B}{h}(k_B T)\frac{L k_0}{l_B^4 n_B}. \tag{10}$$

In units of the quantum of thermal conductance [34, 35] $G_{\rm th}^Q = \dfrac{\pi^2}{3}\dfrac{k_B (k_B T)}{h}$ we can rewrite Eqn. (11) to be

$$\kappa_{zzz}^{UQ} = G_{\rm th}^Q n_{modes}, \tag{11}$$

where n_{modes} is given by

$$n_{modes} = N_p \frac{L k_0}{l_B^4 n_B} \tag{12}$$

can be interpreted as the number of modes per unit magnetic length. In the ultra-quantum limit, we see that the chiral Landau levels provide individual channels of thermal transport, allowing for a direct probe of the quantum of thermal conductance.

Unlike the semiclassical case, we see that the thermal conductivity in the ultra-quantum regime is quadratic in field and has a linear temperature dependence so long as $k_B T \ll \frac{\hbar v_F}{l_B}$. As the upper limit is approached, higher Landau levels become thermally populated, allowing them to also engage in Fermi arc-mediated magnetothermal transport. The motion of charge through the bulk is dictated by the continuity of charge current arising from motion on the arcs. Hence, any scattering between the chiral and conventional Landau levels would be intranodal in nature which should not affect motion of charge through the bulk.

Landauer conductances in the ultra-quantum regime

As in the semiclassical regime above, we can use the Landauer framework to find the electrical conductance in the ultra-quantum limit. We find that

$$\mathcal{M}(\mathcal{E})\mathcal{T}(\mathcal{E}) = \frac{N_P}{\pi}\frac{1}{n_B v_F l_B^2}\frac{dN}{dt}. \tag{13}$$

We use Eqn. (13) to also evaluate the electrical conductance given by Eqn. (6) to obtain

$$G^{UQ} = \frac{2N_P}{\pi}\frac{e^2}{\hbar}\frac{1}{n_B v_F l_B^2}\frac{dN}{dt}. \tag{14}$$

As in the semiclassical regime, we can again calculate the Lorenz number in the ultra-quantum regime

$$L^{UQ} = \frac{\kappa_{zzz}^{UQ}}{T\sigma_{zzz}^{UQ}} = \frac{\pi^2}{3}\left(\frac{k_B}{e}\right)^2. \tag{15}$$

We see that in the ultra-quantum limit, the conventional dimensionless prefactor of $\frac{\pi^2}{3}$ is found in L^{UQ} which reflects occupation of only the chiral $n = 0$ Landau level.

Intermediate regime

In order to investigate the crossover from the low-field semiclassical limit to the ultra-quantum limit of only chiral Landau levels, we include quantum effects of nonchiral higher Landau levels. In this intermediate field regime, the density of states for a pair of Weyl nodes in a mag-

	T-dep	B-dep	L-dep
Arcs (S)	$\kappa^S_{zzz} \sim T^3$	$\kappa^S_{zzz} \sim B$	$\kappa^S_{zzz} \sim L$
Arcs (UQ)	$\kappa^{UQ}_{zzz} \sim T$	$\kappa^{UQ}_{zzz} \sim B^2$	$\kappa^{UQ}_{zzz} \sim L$
Bulk	$\kappa^{\text{bulk}}_{zzz} \sim T^3$	$\kappa^{\text{bulk}}_{zzz} \sim B^2$	$\kappa^{\text{bulk}}_{zzz} \sim L^0$

TABLE I. Summary of temperature, magnetic field, and length dependence of arc-mediated κ_{zzz} in the semiclassical and ultra-quantum limits as well as the bulk semiclassical magnetothermal conductivity.

netic field,

$$g_{LL}(\mathcal{E}) = \frac{B}{\Phi_0}\int_{-\Lambda}^{\Lambda}\frac{dk_z}{2\pi}\Big(\delta(\mathcal{E}-|\mathcal{E}_0|)+\delta(\mathcal{E}+|\mathcal{E}_0|) + 2\sum_n\big(\delta(\mathcal{E}-|\mathcal{E}_n|)+\delta(\mathcal{E}+|\mathcal{E}_n|)\big)\Big), \quad (16)$$

where $\mathcal{E}_n$ is given by Eqn. (9).

We numerically obtain the specific heat and magnetothermal conductivity (see Appendix C) shown in Fig. 3 with contributions from all Landau levels as a function of field for several temperatures. At high temperature, we see a crossover between linear field dependence to quadratic field dependence of the specific heat as the field is increased and only the lowest Landau level becomes occupied. We summarize the field and temperature dependence of the arc-mediated κ_{zzz} in Table I.

The magnetic length is given by $l_B = \frac{25\text{nm}}{\sqrt{B[\text{Tesla}]}}$. Hence, for a typical Weyl semimetal with Fermi velocity $v_F = 10^5\frac{\text{m}}{\text{s}}$, the ultraquantum limit is accessed at temperatures $k_BT \ll \frac{\hbar v_F}{l_B} \sim 10\text{meV}\sqrt{B[\text{Tesla}]}$.

We note that when the chemical potential does not lie at the Weyl nodes, the specific heat will contain quantum oscillations just as is experimentally observed in the bulk κ_{xxz} response of NbP by Stockert *et al.*[46]. However, these quantum oscillations arise purely from the bulk Weyl pockets and will also be present in the specific heat and thermal conductivity in other orientations of applied magnetic field and temperature gradient. We emphasize that it is the non-oscillatory component of the magnetothermal conductivity that will contain signatures of Fermi arc-mediated entropy transport. We point out that in Eqns. (4) and (11), the thermal conductivity is proportional to L, meaning that the ratio κ/L, the areal conductance, is really the intrinsic quantity that does not depend on the sample's dimension along the z-axis.

COMPARISON WITH BULK THERMAL CONDUCTIVITY OF WSM

The bulk thermal conductivity for a Weyl node of chirality χ is given by [29]

$$\kappa^{\text{bulk}}_{zzz} = \int\frac{d^3k}{(2\pi)^3}D\left(\mathbf{B},\mathbf{\Omega}^\chi_{\mathbf{k}}\right)\tau\frac{v_F^2}{3} \times\left(1+l_B^{-2}|\Omega^\chi_{\mathbf{k}}|^2\right)\frac{(\mathcal{E}-\mu)^2}{T}\left(-\frac{\partial f_0}{\partial\mathcal{E}}\right), \quad (17)$$

where $D\left(\mathbf{B},\mathbf{\Omega}^\chi_{\mathbf{k}}\right) = \left(1+2\pi\frac{\mathbf{B}\cdot\mathbf{\Omega}^\chi_{\mathbf{k}}}{\Phi_0}\right)^{-1}$, τ is the scattering time, l_B is the magnetic length, f_0 is the equilibrium Fermi distribution, and $\mathbf{\Omega}^\chi_{\mathbf{k}} = \frac{\chi}{2}\frac{\mathbf{k}}{k^3}$ is the chirality-dependent Berry curvature of the bulk Weyl nodes. To obtain the full magnetothermal conductivity of the bulk, we sum over pairs of nodes of opposite chirality. At zero field and for $\mu \to 0$, we obtain the bulk thermal conductivity from Eqn. (17) to be

$$\kappa^{\text{bulk}}_{zzz}(B=0) = \frac{7\pi^2}{45}N_p(k_Bv_{_F}\Lambda^2)(v_{_F}\tau\Lambda)\Theta^3, \quad (18)$$

as shown in table I. Here, instead of the cutoff Λ we can equally well use the Brillouin zone size $2\pi/a$, but we prefer to leave it in terms of the cutoff to compare with the arc contribution below.

For small values of field $\frac{\hbar v_{_F}}{l_Bk_BT} \ll 1$, the bulk thermal conductivity is

$$\kappa^{\text{bulk}}_{zzz}(B) = \frac{N_p}{3\pi^2}(k_Bv_{_F}\Lambda^2)(v_{_F}\tau\Lambda)\Theta^3\left(\frac{7\pi^4}{15}+\left(\frac{\hbar v_{_F}}{l_Bk_BT}\right)^4\right). \quad (19)$$

The enhancement of $\kappa^{\text{bulk}}_{zzz}$ in a magnetic field is related to the chiral anomaly, and is a consequence of the negative magnetoresistance in Weyl semimetals. By combining the bulk and arc contributions, we obtain the total thermal conductivity,

$$\kappa(B) = (k_Bv_{_F}\Lambda^2)\Theta^3\Bigg((v_{_F}\tau\Lambda)\left[\frac{7\pi^2}{45}+\frac{1}{3\pi^2}\left(\frac{\hbar v_{_F}}{l_Bk_BT}\right)^4\right]+ \frac{14\pi^2}{15}\left(\frac{L}{l_B}\right)\left(\frac{k_0}{l_B\Lambda^2}\right)\Bigg). \quad (20)$$

We recognize the third term to be from the arcs given by Eqn. (4). The field independent term can be easily separated, and the term from the bulk proportional to B^2 is suppressed by a factor of $\left(\frac{\hbar v_{_F}}{l_Bk_BT}\right)^4$. Therefore, we expect the arc-mediated term to be the dominant magnetic field-dependent term.

It is useful to compare the thermal conductivity of the

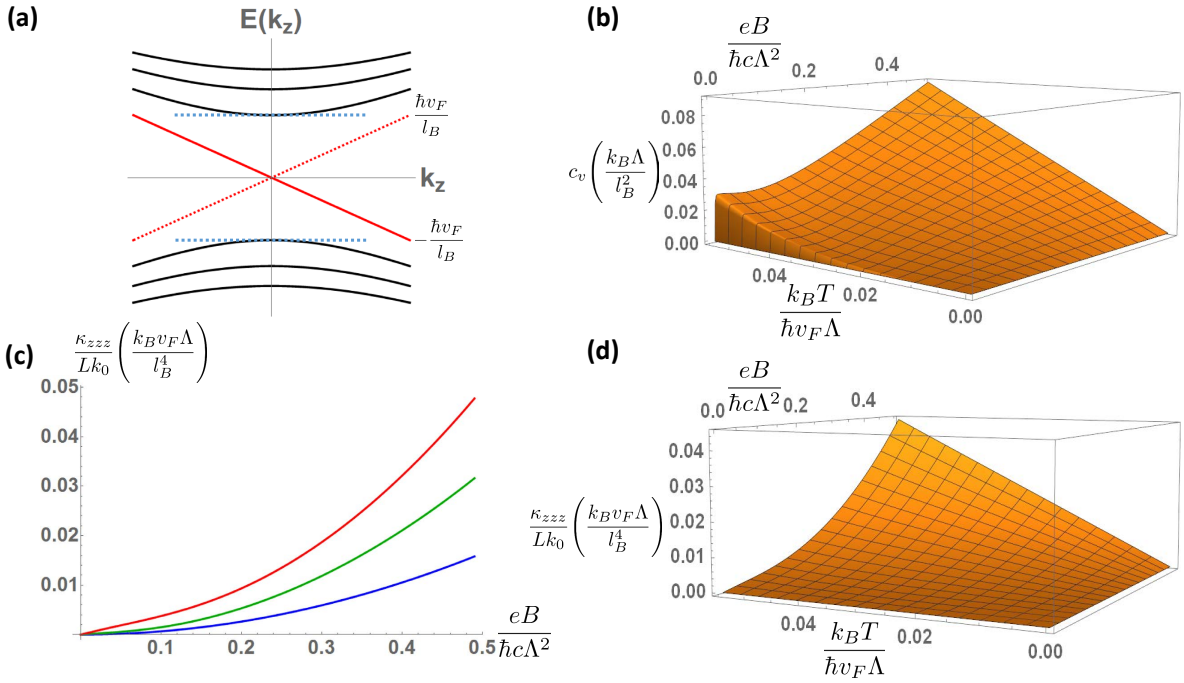

FIG. 3. (a) Schematic of the Landau levels. Chiral $n = 0$ Landau levels (in red) with positive (negative) slope $\chi = 1$ ($\chi = -1$); non-chiral Landau levels ($n \neq 0$) (in black). (b,c) Specific heat c_v and magnetothermal conductivity κ_{zzz} for a single pair of Weyl nodes in the intermediate quantum limit as a function magnetic field (Landau level cutoff $N_{\max} = 50$ and electron density $n_B = 1$). The temperature $\Theta \equiv \frac{k_B T}{\hbar v_F \Lambda} = 0.02$ (blue), 0.04 (green), and 0.06 (red). At higher temperatures (red), we see a crossover between the linear to quadratic low-field behavior when the ultra-quantum limit is reached. At lower temperatures (green, blue) only the lowest Landau level is populated in the field range shown. (d) Fermi arc-mediated magnetothermal conductivity for a single pair of Weyl nodes in the intermediate quantum limit as a function of magnetic field. Parameters are the same as in (b,c).

WSM with that of free electrons at low temperatures for which $\kappa^{free} \sim c_v v_F \ell \sim k_B^2 T g(\epsilon_F) v_F \ell$, where c_v is the free electron specific heat and ℓ is the temperature-independent mean free path due to elastic scattering. Substituting for the density of states $g(\epsilon_F)$ we obtain, $\kappa^{free} \sim 10^2 (\mathrm{Wm^{-1}K^{-1}})(k_B T/\epsilon_F)$. The scale for κ in a bulk WSM is set by $k_B v_F (2\pi/a)^2 \approx 10^2$ $\mathrm{Wm^{-1}K^{-1}}$ where we have used $v_F \sim 3 \times 10^5 \frac{\mathrm{m}}{\mathrm{s}} \sim c/10^3$ and the lattice constant $a \sim 0.3$nm. Notice that this scale is close to the prefactor of κ^{free}. Now the other dimensionless factors contributing to κ^{bulk} are $v_F \tau (2\pi/a) \approx 200$ and $\hbar v_F / l_B k_B T \approx 10$ meV$\sqrt{B(T)[\mathrm{Tesla}]}/k_B T$, where we have used the magnetic length estimate $l_B \approx 25\mathrm{nm}/\sqrt{B(T)[\mathrm{Tesla}]}$. We therefore estimate the bulk $\kappa_{zzz}^{bulk} \approx 10^2 (\mathrm{Wm^{-1}K^{-1}}) 10 N_p (k_B T/4\mathrm{eV})^3$. Against this bulk term, we compare the additional arc contribution which is enhanced by the factor $(L/l_B) \times (1/l_B \Lambda)$ and should be experimentally measurable. We also point out that the bulk thermal conductivity in Eq. (19) is intrinsically volume-independent, whereas the arc conductivity is a surface property: therefore, in Eq. (20), the dependence of heat transport on the dimension of the samples along the z-axis will differentiate the different contributions experimentally.

DISCUSSION AND SUMMARY

Arc-Mediated Entropy Transport in Dirac Semimetals:

In Dirac semimetals[47, 48], observed[49, 50] in Na_3Bi and Cd_3As_2, nodes of opposite chirality coexist at the same momenta but are protected from annihilation with each other by symmetry [51]. Because each Dirac node is comprised of a pair of opposite chirality, each real space surface of a Dirac semimetal has a pair of Fermi arcs for each pair of Dirac nodes. It has been shown that these double Fermi arcs are not topologically protected, in general,[52], except on planes in the surface Brillouin zone which preserve time-reversal invariance. We show different cases for surface states of Dirac semimetals in Fig. 4. Although Fermi arcs may terminate on projections of Dirac nodes (Fig. 4a), it is possible for perturbations that break no symmetries of the Dirac semimetal to deform the surface Fermi arcs into closed Fermi pockets on the surface (Fig. 4b). Doping the system away from the Dirac point may not change the nature of these closed Fermi pockets (Fig. 4c) unless the doping is large enough for the bulk Fermi pockets to grow and mix with the surface states, restoring the arcs (Fig. 4d).

In cases (b) and (c) above, the topologically trivial

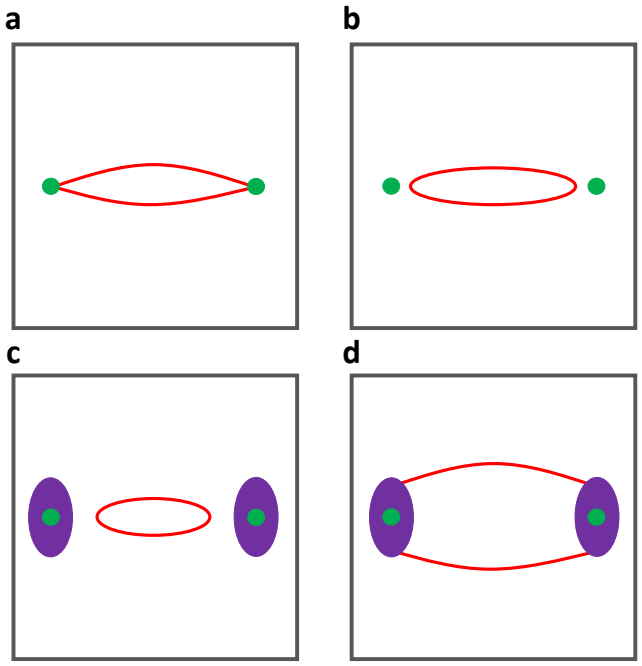

FIG. 4. Schematic of the different cases for surface states in a Dirac semimetal with a single pair of Dirac nodes[52]. Green dots represent projections of the Dirac nodes on the surface Brillouin zone. Red contours are surface states on a single surface. Purple filled regions represent projections of bulk Fermi pockets which enclose Dirac nodes. In (a-b), the Fermi energy is at the Dirac nodes, while in (c-d) the Fermi energy is doped away from the Dirac nodes. (a) A pair of surface Fermi arcs terminates on the Dirac nodes on a single surface. (b) A perturbation containing the full symmetry of the full Dirac Hamiltonian which does not shift the bulk Dirac nodes can deform the Fermi arcs into a closed Fermi pocket on the surface, much like a topological insulator. (c) When the Fermi energy is shifted away from the Dirac nodes, the surface states may still form a closed Fermi pocket. (d) Sufficient doping may cause the Fermi pockets to grow large enough for the surface states to merge with the bulk pockets.

nature of the surface states negates the possibility of Fermi arc-mediated entropy transport discussed in this work. The cases (a) and (d) are more interesting. In these cases, we have two copies of the conveyor belt orbits shown in Fig. 1. Hence, we obtain the same results for the arc-mediated magnetothermal conductivity of a Dirac semimetal as in Eqn. (4) and (11) by setting N_p to be twice the number of pairs of Dirac nodes. Case (d) above may be the most physically relevant. In quantum oscillation experiments on thin films of Cd_3As_2, there is evidence that the observed Shubnikov-de Haas oscillations arise from combinations of bulk Landau levels and surface Fermi arcs [24, 26]. This opens the door for studies of Fermi arc-mediated entropy transport in Dirac semimetals.

Effect of disorder: We have tacitly assumed in the discussion above that we are justified in ignoring scattering

Material	$v_F\left(\frac{\mathrm{m}}{\mathrm{s}}\right)$	N_p
TaAs[21]	3×10^5	12
TaP[23, 53]	3×10^5	12
NbAs[54, 55]	6×10^5	12
NbP[56]	4.8×10^5	12
Cd_3As_2[57, 58]	1.5×10^6	2
Na_3Bi[59]	7.5×10^5	2

TABLE II. Several topological semimetal candidates for Fermi arc-mediated entropy transport. Since Cd_3As_2 and Na_3Bi are Dirac semimetals, the number of Weyl nodes N_p reported is double the number of Dirac nodes.

effects given the topological nature of the Fermi arc mediated entropy flow. Here, we justify that assumption in some detail. We must consider (i) scattering of electrons on the Fermi arcs, (ii) scattering within a bulk Weyl node (intra-nodal), and (iii) scattering between nodes (internodal) scattering.

(i) Scattering on the arcs is suppressed by the small density of states of the linearly dispersing Fermi arcs. As seen by a Golden rule argument, the scattering rate $\frac{1}{\tau_{\mathrm{arc}}}(\mathbf{k}) \sim \sum_{\mathbf{k}'} \mathbf{g_A}(\mathcal{E}_{\mathbf{k}'})|\langle\mathbf{k}|\mathbf{V}|\mathbf{k}'\rangle|^{\mathbf{2}}$, where $V(\mathbf{r})$ is the impurity potential and the density of states on the arc is given by $g_A(\mathcal{E}_{\mathbf{k}}) = \frac{k_0}{\hbar v_F}$. For multiple pairs of Weyl nodes, with more than one Fermi arc on each surface, scattering between arcs is possible, and, for materials with closely spaced arcs in the surface Brillouin zone such scattering could suppress the arc-mediated thermal transport. Thus, ideal materials are those with single pairs of Weyl nodes, or those with well-isolated Fermi arcs in the surface Brilllouin zone.

(ii) At finite temperatures, the width of the bulk channel is $\Delta k \sim \frac{k_B T}{\hbar v_F}$. Even in the presence of any intra-nodal scattering, charge and heat will continue to drift within this channel dictated by the continuity equation.

(iii) At low temperatures, short-ranged impurities can provide the large momentum transfers to scatter electrons from one node to the other. Internode scattering from slowly varying potentials or phonons is suppressed at low temperatures $k_B T \ll \hbar\omega_D$ because only small momenta phonons can be excited at these temperatures that would typically contribute to inelastic scattering within a given pocket. This phase space argument also rules out phonon drag contributions, since for most known Weyl semimetals, the Fermi energy is small compared to the Debye energy $E_F \ll \hbar\omega_D$, suppressing the number of states available for phonon scattering and phonon drag as pointed out by Stockert *et al.*[46].

Experimental implications:

We summarize the transport properties of some candidate materials for Fermi arc-mediated entropy transport in Table II. Although weak spin-orbit coupling compared

to the tantalum monopnictides causes the Weyl nodes to be closer together in NbP and NbAs, they still appear to be promising cadidates with high Fermi velocities. The Dirac semimetal Cd_3As_2 has been shown to possess putative Shubnikov-de Haas oscillations that arise from combinations of bulk Landau levels and surface Fermi arcs [24, 26]. We predict that Fermi arc-mediated entropy transport would be an even stronger transport signature of topological Fermi arcs in these materials.

We have considered orientations of magnetic fields perpendicular to the surface Brillouin zone in which Fermi arcs reside. In systems which preserve time-reversal symmetry, there must be only a single pair of such surfaces that have Fermi arcs. On all of the other surfaces, Weyl nodes of opposite chirality will project on top of one another and therefore not lead to Fermi arcs. When the magnetic field is applied along such a direction, there will be no contribution to the magnetothermal conductivity from the Fermi arcs and no such conveyor-belt transport of entropy. Although the bulk electronic pockets as well as phonons may contribute to the thermal conductivity in these other magnetic field configurations, we have argued above that the contribution of arc-mediated entropy transport in the cofiguration shown in Fig. 1b will likely be stronger than these other contributions. This will lead to a clear anisotropy between directions with Fermi arcs and without Fermi arcs.

CONCLUSION AND FURTHER DIRECTIONS

In conclusion, we have shown that in the presence of a magnetic field and temperature gradient, each applied perpendicular to the surface Brillouin zone of a Weyl semimetal, the Lorentz force on the Fermi arcs leads to a conveyor belt motion of charge and a net flow of heat. This heat flow leads to a highly anisotropic magnetothermal conductivity that has distinct behaviors in the semiclassical and quantum regimes, and can be separated from the bulk contribution.

Type II Weyl semimetals: In this paper, we have focused on type I topological semimetals, but recently a second class, known as type II Weyl and Dirac semimetals, have been theoretically predicted [60–63] and observed in several candidate materials[64–68]. Type II WSMs have non-vanishing density of states at the Weyl points and can be understood as the limiting case of an indirect gap semiconductor where the gap closes at the Weyl nodes. The tilted nodes in type II WSMs lead to several distinct characteristics, perhaps most notably the lack of chiral Landau levels when the magnetic field is applied outside of the tilt cone[60, 69]. Due to the extended nature of the Fermi pockets that meet at the Weyl nodes, lattice models[39] are needed to accurately describe their properties rather than the continuum models used for most of the analysis in this work. We leave an investigation of Fermi arc mediated magnetothermal conductivity in type II WSMs for future work.

Applications: We point out that conveyor-belt thermal transport could potentially find applications in magnetically actuated all-solid-state thermal switches. Presently, most thermal switches are mechanical or involve exchange gases, because all-solid-state switches have either low switching ratios or work over only a limited temperature range. Here we suggest that the amplitude or the direction of an external magnetic field can affect a change in a Weyl semimetal from an "on" state where arcs contribute to entropy transport to an "off" state where they do not. Given the highly directional nature of the entropy transport, we expect it to be relatively immune from scattering. We further expect to achieve high switching ratios and a large operating temperature range by adjusting the sample length, as long as the phonon contribution to the total conductivity is not too large.

ACKNOWLEDGMENTS

We would like to thank M. Crommie and A. C. Potter for useful discussions. T. M. M. and J. P. H. were supported by the Center for Emergent Materials, an NSF MRSEC, under grant DMR-1420451. S. J. W. was supported by the National Science Foundation Graduate Research Fellowship Program under Grant No. DGE-0822215. N. T. acknowledges funding from NSF-DMR-1309461.

APPENDIX: HEAT CAPACITY OF WEYL NODES

A: semiclassical regime

The energy density $u = U/V$ of Weyl nodes is:

$$u = \int_{-\hbar v_F \Lambda}^{\hbar v_F \Lambda} d\mathcal{E} \frac{\mathcal{E}\ g(\mathcal{E})}{1 + e^{\beta(\mathcal{E}-\mu(T))}} = \frac{1}{\pi^2(\hbar v_F)^3} \int_{-\hbar v_F \Lambda}^{\hbar v_F \Lambda} d\mathcal{E} \frac{\mathcal{E}^3}{1 + e^{\frac{\mathcal{E}-\mu(T)}{k_B T}}}, \quad (21)$$

where V is the volume and Λ is a momentum regularization which is set by the separation of the Weyl nodes in momentum-space. It is useful to define a dimensionless temperature $\Theta = \frac{k_B T}{\hbar v_F \Lambda}$ in units of the energy cut off. For the case when $\mu(T) \to 0$

$$u = \frac{1}{\pi^2}(k_B T)\Theta^3 \int_{-\frac{1}{\Theta}}^{\frac{1}{\Theta}} dx \frac{x^3}{1 + e^x}. \quad (22)$$

This integral can be evaluated in terms of the polylogarithm function of order s, $\mathrm{Li}_s(z) = \sum_{k=1}^{\infty} \frac{z^k}{k^s}$ for complex z such that $|z| < 1$. The heat capacity is given by:

$$\frac{du}{dT} = \frac{\Lambda^3 k_B}{\pi^2}\Bigg(-\Theta^3\Bigg(\frac{7}{15} + \mathrm{Li}_4\left(-e^{\frac{1}{\Theta}}\right)\Bigg) + \frac{2}{\Theta}\frac{1}{1+e^{\frac{1}{\Theta}}} - 8\ln\left(1+e^{\frac{1}{\Theta}}\right) - 24\Theta\mathrm{Li}_2\left(-e^{\frac{1}{\Theta}}\right) + 48\Theta^2\mathrm{Li}_3\left(-e^{\frac{1}{\Theta}}\right)\Bigg). \quad (23)$$

For temperatures such that $\Theta \lesssim 0.4$, it can be shown that

$$\frac{du}{dT} \approx \frac{c_0}{\pi^2}\Lambda^3 k_B \Theta^3, \quad (24)$$

where $c_0 = \frac{7\pi^4}{15}$ is a purely numerical constant. We can also rewrite it in terms of the energy per particle as: $\frac{dE}{dT}$ from Eqn. (24) to be

$$\frac{dE}{dT} = c_0 \frac{k_B \Theta^3}{\pi^2 n_B}, \quad (25)$$

where $n_B = \frac{N}{V}$ is the density.

B: ultra-quantum regime

In the ultraquantum regime, only the $n = 0$ Landau level participates in entropy transport. In Eq.21 the internal energy is given in terms of g_0, the density of states of the zero energy Landau levels

$$g_0(\mathcal{E}) = \frac{B}{\Phi_0}\int_{-\Lambda}^{\Lambda}\frac{dk_z}{2\pi}\Big(\delta(\mathcal{E} - |\mathcal{E}_0|) + \delta(\mathcal{E} + |\mathcal{E}_0|)\Big), \quad (26)$$

where $\mathcal{E}_0$ is the energy of the chiral Landau level. Here $\Phi_0 = \frac{hc}{e}$ is the quantum of magnetic flux. The internal energy density from both nodes is:

$$u_0 = \frac{B}{\Phi_0}\hbar v_F \int_{-\Lambda}^{\Lambda}\frac{dk_z}{2\pi}\Bigg(\frac{k_z}{1+e^{\beta(\hbar v_F k_z - \mu)}} - \frac{k_z}{1+e^{\beta(-\hbar v_F k_z - \mu)}}\Bigg), \quad (27)$$

which can be evaluated to obtain

$$\frac{du_0}{dT} = \frac{k_B \Lambda B}{\pi \Phi_0}\Bigg(\frac{4}{\Theta}\frac{1}{1+e^{-\frac{1}{\Theta}}} - 8k_B\Lambda\ln\Big(1+e^{\frac{1}{\Theta}}\Big) + 2\Theta\Big(\frac{\pi^2}{3} + 4\mathrm{Li}_2\Big(-e^{\frac{1}{\Theta}}\Big)\Big)\Bigg), \quad (28)$$

where $\mathrm{Li}_s(z)$ is the polylogarithm function of order s.

In the low temperature limit $\Theta \ll 1$, we find that the specific heat is

$$\frac{du_0}{dT} \approx \frac{2\pi}{3}\frac{\Lambda k_B}{\Phi_0}\Theta B\,. \quad (29)$$

C: crossover regime

From Eqn. (16), the additional internal energy can be calculated by

$$\widetilde{u} = 2\frac{B}{\Phi_0}\frac{\hbar v_F}{l_B}\sum_n \int_{-\Lambda}^{\Lambda}\frac{dk_z}{2\pi}h(k_z,n) \Bigg(\frac{1}{1+e^{(\beta\hbar v_F/l_B)(h-\mu)}} - \frac{1}{1+e^{-(\beta\hbar v_F/l_B)(h-\mu)}}\Bigg), \quad (30)$$

where $h(k_z, n) = \sqrt{|n| + k_z^2 l_B^2}$. The total energy density is now given by the sum of Eqns. (27) and (30) to obtain $u_{\mathrm{tot}} = u_0 + \widetilde{u}$. Unlike Eqn. (27), the expression above for $\widetilde{u}$ cannot be evaluated analytically. Instead, we evaluate Eqn. (30) numerically by introducing a regularization $N_{\max}$ which cuts off the sum over Landau levels. We take the system to be at charge neutrality where $\mu = 0$. We can then calculate the specific heat by numerically evaluating derivatives with respect to temperature.

* mccormick.288@osu.edu
† trivedi.15@osu.edu

[1] M. Z. Hasan and C. L. Kane, Rev. Mod. Phys. **82**, 3045 (2010).
[2] X.-L. Qi and S.-C. Zhang, Rev. Mod. Phys. **83**, 1057 (2011).
[3] A. A. Burkov and L. Balents, Phys. Rev. Lett. **107**, 127205 (2011).
[4] X. Wan, A. M. Turner, A. Vishwanath, and S. Y. Savrasov, Phys. Rev. B **83**, 205101 (2011).
[5] G. Xu, H. Weng, Z. Wang, X. Dai, and Z. Fang, Phys. Rev. Lett. **107**, 186806 (2011).
[6] G. Volovik and M. Zubkov, Nuclear Physics B **881**, 514 (2014).
[7] S.-Y. Xu, I. Belopolski, N. Alidoust, M. Neupane, G. Bian, C. Zhang, R. Sankar, G. Chang, Z. Yuan, C.-C. Lee, S.-M. Huang, H. Zheng, J. Ma, D. S. Sanchez, B. Wang, A. Bansil, F. Chou, P. P. Shibayev, H. Lin, S. Jia, and M. Z. Hasan, Science **349**, 613 (2015).
[8] B. Q. Lv, H. M. Weng, B. B. Fu, X. P. Wang, H. Miao, J. Ma, P. Richard, X. C. Huang, L. X. Zhao, G. F. Chen, Z. Fang, X. Dai, T. Qian, and H. Ding, Phys. Rev. X **5**, 031013 (2015).
[9] B. Q. Lv, N. Xu, H. M. Weng, J. Z. Ma, P. Richard, X. C. Huang, L. X. Zhao, G. F. Chen, C. E. Matt, F. Bisti, V. N. Strocov, J. Mesot, Z. Fang, X. Dai, T. Qian, M. Shi, and H. Ding, Nat Phys **11**, 724 (2015).

[10] H. Nielsen and M. Ninomiya, Physics Letters B **105**, 219 (1981).

[11] A. H. Castro Neto, F. Guinea, N. M. R. Peres, K. S. Novoselov, and A. K. Geim, Rev. Mod. Phys. **81**, 109 (2009).

[12] P. Hosur, S. A. Parameswaran, and A. Vishwanath, Phys. Rev. Lett. **108**, 046602 (2012).

[13] D. T. Son and B. Z. Spivak, Phys. Rev. B **88**, 104412 (2013).

[14] Y. Chen, S. Wu, and A. A. Burkov, Phys. Rev. B **88**, 125105 (2013).

[15] H.-J. Kim, K.-S. Kim, J.-F. Wang, M. Sasaki, N. Satoh, A. Ohnishi, M. Kitaura, M. Yang, and L. Li, Phys. Rev. Lett. **111**, 246603 (2013).

[16] K.-S. Kim, H.-J. Kim, and M. Sasaki, Phys. Rev. B **89**, 195137 (2014).

[17] E. V. Gorbar, V. A. Miransky, and I. A. Shovkovy, Phys. Rev. B **89**, 85126 (2014).

[18] J. Klier, I. V. Gornyi, and A. D. Mirlin, Phys. Rev. B **92**, 205113 (2015).

[19] P. Goswami, J. H. Pixley, and S. Das Sarma, Phys. Rev. B **92**, 75205 (2015).

[20] B. Z. Spivak and A. V. Andreev, Phys. Rev. B **93**, 085107 (2016).

[21] X. Huang, L. Zhao, Y. Long, P. Wang, D. Chen, Z. Yang, H. Liang, M. Xue, H. Weng, Z. Fang, X. Dai, and G. Chen, Phys. Rev. X **5**, 31023 (2015).

[22] C.-L. Zhang, S.-Y. Xu, I. Belopolski, Z. Yuan, Z. Lin, B. Tong, G. Bian, N. Alidoust, C.-C. Lee, S.-M. Huang, T.-R. Chang, G. Chang, C.-H. Hsu, H.-T. Jeng, M. Neupane, D. S. Sanchez, H. Zheng, J. Wang, H. Lin, C. Zhang, H.-Z. Lu, S.-Q. Shen, T. Neupert, M. Zahid Hasan, and S. Jia, Nature Communications **7**, 10735 (2016).

[23] F. Arnold, C. Shekhar, S.-c. Wu, Y. Sun, R. D. dos Reis, N. Kumar, M. Naumann, M. O. Ajeesh, M. Schmidt, A. G. Grushin, J. H. Bardarson, M. Baenitz, D. Sokolov, H. Borrmann, M. Nicklas, C. Felser, E. Hassinger, and B. Yan, Nat Commun **7**, 11615 (2016).

[24] A. C. Potter, I. Kimchi, and A. Vishwanath, Nat Commun **5**, 1 (2014).

[25] Y. Zhang, D. Bulmash, P. Hosur, A. C. Potter, and A. Vishwanath, Scientific Reports **6**, 23741 (2016).

[26] P. J. W. Moll, N. L. Nair, T. Helm, A. C. Potter, I. Kimchi, A. Vishwanath, and J. G. Analytis, Nature **535**, 266 (2016).

[27] J. Borchmann and T. Pereg-Barnea, (2017), arXiv:1704.07282.

[28] Y. Baum, E. Berg, S. A. Parameswaran, and A. Stern, Phys. Rev. X **5**, 41046 (2015).

[29] R. Lundgren, P. Laurell, and G. A. Fiete, Phys. Rev. B **90**, 165115 (2014).

[30] G. Sharma, P. Goswami, and S. Tewari, Phys. Rev. B **93**, 035116 (2016).

[31] A. Lucas, R. A. Davison, and S. Sachdev, Proceedings of the National Academy of Sciences **113**, 9463 (2016).

[32] Q. Chen and G. A. Fiete, Phys. Rev. B **93**, 155125 (2016).

[33] S. J. Watzman, T. M. McCormick, C. Sekhar, S.-C. Wu, Y. Sun, A. Prakash, C. Felser, N. Trivedi, and J. P. Heremans, (2017), arXiv:1703.04700.

[34] J. B. Pendry, Journal of Physics A: Mathematical and General **16**, 2161 (1983).

[35] K. Schwab, E. A. Henriksen, J. M. Worlock, and M. L. Roukes, Nature **404**, 974 (2000).

[36] T. C. Harman and J. M. Honig, *Thermoelectric and Thermomagnetic Effects and Applications* (McGraw-Hill, 1967).

[37] C. F. Gallo, B. S. Chandrasekhar, and P. H. Sutter, Journal of Applied Physics **34**, 144 (1963).

[38] K.-Y. Yang, Y.-M. Lu, and Y. Ran, Phys. Rev. B **84**, 075129 (2011).

[39] T. M. McCormick, I. Kimchi, and N. Trivedi, Phys. Rev. B **95**, 075133 (2017).

[40] See Supplemental Material at [URL will be inserted by publisher] for more details of the Fermi arc occupations.

[41] R. Landauer, IBM Journal of Research and Development **1**, 223 (1957).

[42] R. Landauer, Journal of Physics: Condensed Matter **1**, 8099 (1989).

[43] S. Datta, *Lessons from Nanoelectronics: A New Perspective on Transport* (World Scientific Publishing Company, 2012).

[44] M. Lundstrom and J. Changwook, *Near-Equilibrium Transport: Fundamentals and Applications* (World Scientific Publishing Company, 2013).

[45] K. Behnia, *Fundamentals of Thermoelectricity* (Oxford University Press, 2015).

[46] U. Stockert, R. D. dos Reis, M. O. Ajeesh, S. J. Watzman, M. Schmidt, C. Shekhar, J. P. Heremans, C. Felser, M. Baenitz, and M. Nicklas, (2017), arXiv:1704.02241.

[47] Z. Wang, Y. Sun, X.-Q. Chen, C. Franchini, G. Xu, H. Weng, X. Dai, and Z. Fang, Phys. Rev. B **85**, 195320 (2012).

[48] Z. Wang, H. Weng, Q. Wu, X. Dai, and Z. Fang, Phys. Rev. B **88**, 125427 (2013).

[49] Z. K. Liu, J. Jiang, B. Zhou, Z. J. Wang, Y. Zhang, H. M. Weng, D. Prabhakaran, S.-K. Mo, H. Peng, P. Dudin, T. Kim, M. Hoesch, Z. Fang, X. Dai, Z. X. Shen, D. L. Feng, Z. Hussain, and Y. L. Chen, Nat Mater **13**, 677 (2014).

[50] Z. K. Liu, B. Zhou, Y. Zhang, Z. J. Wang, H. M. Weng, D. Prabhakaran, S.-K. Mo, Z. X. Shen, Z. Fang, X. Dai, Z. Hussain, and Y. L. Chen, Science **343**, 864 (2014).

[51] S. M. Young, S. Zaheer, J. C. Y. Teo, C. L. Kane, E. J. Mele, and A. M. Rappe, Phys. Rev. Lett. **108**, 140405 (2012).

[52] M. Kargarian, M. Randeria, and Y.-M. Lu, Proceedings of the National Academy of Sciences **113**, 8648 (2016).

[53] S.-Y. Xu, I. Belopolski, D. S. Sanchez, C. Zhang, G. Chang, C. Guo, G. Bian, Z. Yuan, H. Lu, T.-R. Chang, P. P. Shibayev, M. L. Prokopovych, N. Alidoust, H. Zheng, C.-C. Lee, S.-M. Huang, R. Sankar, F. Chou, C.-H. Hsu, H.-T. Jeng, A. Bansil, T. Neupert, V. N. Strocov, H. Lin, S. Jia, and M. Z. Hasan, Science Advances **1** (2015).

[54] S.-Y. Xu, N. Alidoust, I. Belopolski, C. Zhang, G. Bian, T.-R. Chang, H. Zheng, V. Strokov, D. S. Sanchez, G. Chang, Z. Yuan, D. Mou, Y. Wu, L. Huang, C.-C. Lee, S.-M. Huang, B. Wang, A. Bansil, H.-T. Jeng, T. Neupert, A. Kaminski, H. Lin, S. Jia, and M. Z. Hasan, Nat Phys **11**, 748 (2015).

[55] N. J. Ghimire, Y. Luo, M. Neupane, D. J. Williams, E. D. Bauer, and F. Ronning, Journal of Physics: Condensed Matter **27**, 152201 (2015).

[56] C. Shekhar, A. K. Nayak, Y. Sun, M. Schmidt, M. Nicklas, I. Leermakers, U. Zeitler, Y. Skourski, J. Wosnitza, Z. Liu, Y. Chen, W. Schnelle, H. Borrmann, Y. Grin, C. Felser, and B. Yan, Nat Phys **11**, 645 (2015).

[57] M. Neupane, S.-Y. Xu, R. Sankar, N. Alidoust, G. Bian, C. Liu, I. Belopolski, T.-R. Chang, H.-T. Jeng, H. Lin, A. Bansil, F. Chou, and M. Z. Hasan, Nature Communications **5**, 3786 (2014).

[58] T. Liang, Q. Gibson, M. N. Ali, M. Liu, R. J. Cava, and N. P. Ong, Nat Mater **14**, 280 (2015).

[59] S. K. Kushwaha, J. W. Krizan, B. E. Feldman, A. Gyenis, M. T. Randeria, J. Xiong, S.-Y. Xu, N. Alidoust, I. Belopolski, T. Liang, M. Z. Hasan, N. P. Ong, A. Yazdani, and R. J. Cava, APL Materials **3**, 041504 (2015).

[60] A. A. Soluyanov, D. Gresch, Z. Wang, Q. Q.-S. Wu, M. Troyer, X. Dai, and B. A. Bernevig, Nature **527**, 495 (2015).

[61] Y. Sun, S. C. Wu, M. N. Ali, C. Felser, and B. Yan, Phys. Rev. B **92**, 161107 (2015).

[62] Z. Wang, D. Gresch, A. A. Soluyanov, W. Xie, S. Kushwaha, X. Dai, M. Troyer, R. J. Cava, and B. A. Bernevig, Phys. Rev. Lett. **117**, 56805 (2016).

[63] K. Koepernik, D. Kasinathan, D. V. Efremov, S. Khim, S. Borisenko, B. Büchner, and J. van den Brink, Phys. Rev. B **93**, 201101 (2016).

[64] L. Huang, T. M. McCormick, M. Ochi, Z. Zhao, M.-T. Suzuki, R. Arita, Y. Wu, D. Mou, H. Cao, J. Yan, N. Trivedi, and A. Kaminski, Nat Mater **15**, 1155 (2016).

[65] Y. Wu, D. Mou, N. H. Jo, K. Sun, L. Huang, S. L. Bud'Ko, P. C. Canfield, and A. Kaminski, Phys. Rev. B **94**, 121113 (2016).

[66] F. Y. Bruno, A. Tamai, Q. S. Wu, I. Cucchi, C. Barreteau, A. De La Torre, S. McKeown Walker, S. Ricci, Z. Wang, T. K. Kim, M. Hoesch, M. Shi, N. C. Plumb, E. Giannini, A. A. Soluyanov, and F. Baumberger, Phys. Rev. B **94**, 121112 (2016).

[67] C. Wang, Y. Zhang, J. Huang, S. Nie, G. Liu, A. Liang, Y. Zhang, B. Shen, J. Liu, C. Hu, Y. Ding, D. Liu, Y. Hu, S. He, L. Zhao, L. Yu, J. Hu, J. Wei, Z. Mao, Y. Shi, X. Jia, F. Zhang, S. Zhang, F. Yang, Z. Wang, Q. Peng, H. Weng, X. Dai, Z. Fang, Z. Xu, C. Chen, and X. J. Zhou, Phys. Rev. B , 241119 (2016).

[68] G. Chang, S.-Y. Xu, D. S. Sanchez, S.-M. Huang, C.-C. Lee, T.-R. Chang, G. Bian, H. Zheng, I. Belopolski, N. Alidoust, H.-T. Jeng, A. Bansil, H. Lin, and M. Z. Hasan, Science Advances **2** (2016).

[69] S. Tchoumakov, M. Civelli, and M. O. Goerbig, Phys. Rev. Lett. **117**, 086402 (2016).